Journal of Nuclear Materials 605 (2025) 155588

Contents lists available at ScienceDirect

Journal of Nuclear Materials

journal homepage: www.elsevier.com/locate/jnucmat

Self-ion-irradiation-induced grain formation in nickel

S.E. Donnelly [a,*], G. Greaves [a], F. Granberg [b], J. Sharp [a], A.H. Milston [a], J.A. Hinks [a], K. Nordlund [b]

[a] School of Computing and Engineering, University of Huddersfield, HD1 3DH, UK
[b] Department of Physics, P. O. Box 43, FIN-00014 University of Helsinki, Finland

HIGHLIGHTS

- Radiation damage in a cross-sectionally wedge-shaped single-crystal nickel Transmission Electron Microscopy (TEM) foil causes the build-up of stress in the implanted layer;
- Point defects evolve into dislocation with a preferred orientation that leads to a radial bending of the foil;
- MD simulations indicate that radiation damage in Ni with a constrained underlying layer is likely to give rise to the formation of interstitial-type dislocation loops with a preferential orientation that favors the radial bending of the foil as observed experimentally;
- The loops combine to form lines and the lateral stress results in the "pile-up" of these dislocations to form low-angle grain boundaries, converting single-crystal material into long thin grains ≈ 100 – 200 nm in width but > 1 μm in length.
- The width of the grain boundaries is determined by the interaction of glisssile dislocations with the stress induced by the radiation-damaged layer and that from a neighbouring boundary.

GRAPHICAL ABSTRACT

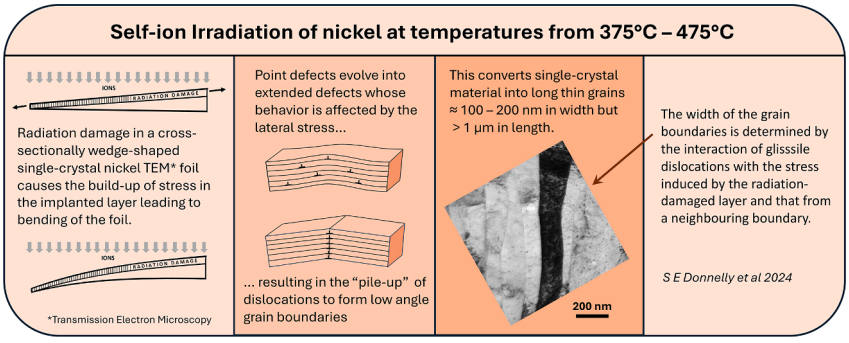

ARTICLE INFO

Keywords:
Nickel
Ni
Transmission Electron Microscopy
Molecular Dynamics
Radiation Damage
Low-angle Grain Boundary

ABSTRACT

A series of experiments has been conducted in which thin foils containing large polycrystals of Ni (single crystals from the perspective of transmission electron microscopy) have been irradiated with 300 keV Ni ions at temperatures from 25° to 475°C. The aim was to examine the fundamental aspects of the build-up of extended defects in a "simple" system with no implantation of foreign species and without the likelihood of segregation, precipitation or formation of new phases. Experiments were carried out using the MIAMI-2 facility in which the development of radiation damage is observed (and recorded) whilst ion-irradiating in-situ in a transmission

* Corresponding author.
E-mail address: s.e.donnelly@hud.ac.uk (S.E. Donnelly).

https://doi.org/10.1016/j.jnucmat.2024.155588
Received 25 September 2024; Received in revised form 1 December 2024; Accepted 22 December 2024
Available online 25 December 2024

electron microscope. Surprisingly, all irradiations of the electrochemically-thinned foils of Ni resulted in the accumulation of dislocations to form low-angle grain boundaries such that single crystal material was converted into a series of grains, each typically less than 200 nm in width but generally more than 1 μm in length with the long axis approximately parallel to the edge of the foil. The early stages of this process have been modelled using Molecular Dynamics simulations and an interpretation of this process of radiation-induced grain-boundary formation is discussed in terms of the coupled effects of irradiation, temperature and stress induced by the radiation damage. The stress arises due to swelling in the thin irradiated region of the jet-polished specimens (with a wedge-shaped radial cross section) which is constrained by deeper-lying unirradiated material. The position in which a grain boundary forms is determined by the interaction of glisssile dislocations with the stress induced by the radiation-damaged layer and that from a neighbouring boundary.

1. Introduction

Ion irradiation of potential materials for nuclear reactors is frequently used as a substitute for the more costly and time-consuming approach of irradiation with neutrons in a nuclear reactor [1]. However, there are differences between the effects of ion and neutron irradiation due in part to the much lower damage rate obtained with neutrons but also due to the production of hydrogen and helium by nuclear transmutation that does not generally take place under ion irradiation. For instance, self-ion irradiation can be used to produce, in hours, the amount of displacement damage that would take years to develop using neutrons; however, the effects of any simultaneous build-up of light gases, particularly helium will be absent in the ion-beam experiments. By employing sequential or simultaneous implantation of helium to appropriate fluences, a better simulation of the overall effects of neutron irradiation can be obtained and, in particular, the nanometre-sized He bubbles, that result from the combination of helium and displacement damage, are observed and can be studied. Such bubbles consist of He combined with lattice vacancies and their formation may result in fewer vacancies being available for recombination with the self-interstitial atoms (SIAs) that are inevitably formed together with the vacancies (Frenkel defects) during the collision cascades induced by the ions or neutrons. The introduction of He into a material together with displacement damage may thus also have a significant effect on the number of surviving self-interstitial atoms (SIAs) and this may result ultimately in a greater concentration of interstitial-type defects such as dislocation loops and lines.

As part of an intended series of experiments to explore this specific issue, we initially performed experiments aimed at studying the extended defects resulting from self-ion irradiation of Ni at different temperatures as a starting point for comparison with subsequent experiments involving irradiation to identical damage levels but with the simultaneous introduction of He. We chose to use Ni in this study as a representative face-centred cubic (FCC) metal and an elemental material which thus enabled us to avoid any potential effects of segregation, precipitation or formation of new phases that might result from experiments on more complex alloys. In the course of this study, however, we made the unexpected discovery that self-ion-irradiation of an electrochemically jet-polished foil of this elemental metal can give rise to the formation of low-angle grain boundaries (LAGB) resulting in the transformation of an initially single crystalline region into a series of narrow grains, elongated in a direction approximately parallel to the foil edge. It is this effect that is the focus of the current study.

Grain *growth* in elemental metallic films induced by ion-irradiation has previously been observed –including in experiments using in-situ observations similar to the present work [2]) and, for instance, in experiments using a Focused Ion Beam (FIB) system where both growth of existing grains and the formation of intermetallic phases were observed [3]. In the more complex environment of nuclear fuels, "subgrain" formation has been reported under neutron irradiation [4] but, in this case, initiation of the grain boundaries was attributed to the interaction of dislocations with fission-product precipitates. Self ion-induced *formation* of grain boundaries in single-crystal elemental materials, however, has not, to our knowledge, been previously observed.

2. Experimental

Discs of Ni, with a nominal purity of 99.99%, 3 mm in diameter were punched out of a polycrystalline foil 125 μm in thickness (from Advent Research Materials Ltd.) and then electrochemically jet-polished using a Struers TenuPol-5 system employing an electrolyte consisting of perchloric acid (60%) 78 ml, water 90 ml, methanol 730 ml, 2-butoxyethanol 100 ml. The specimens were polished simultaneously from both sides using a potential of 35 V between the jet and the specimen with a current typically of 200 mA at a temperature of –30°C. The specimens were immediately removed after perforation and rinsed in three successive baths of methanol. Specimens had a grain size of several microns and the areas studied (always less than 1μm in size) were chosen to be in the centre of individual grains. Experiments were thus carried out on regions of the foils that were initially monocrystalline.

Prior to ion-irradiation, specimens were annealed at 600°C in the TEM. This was done primarily to relieve stresses and remove damage due to handling during specimen preparation and thus ensure that any thermally-induced bending of the foils would already have occurred prior to the irradiations (carried out at lower temperatures). For comparison purposes, an experiment was also carried out on a single-crystal Ni specimen prepared using an FEI Quanta 3D FIB system. This consisted of a lamella (5 × 8 μm and approximately 1–2 μm thick and a thinned electron transparent region ≈ 220 nm in thickness with parallel surfaces (i.e. not wedge-shaped in section). For this sample the conventional in-situ FIB lift-out technique was followed and 30 keV Ga^+ ions were used for the thinning with currents ranging from 7 nA down to 10 pA for the final polishing. Thickness profiles of some specimens were determined by means of Electron Energy Loss (EELS) thickness mapping using a Gatan Imaging Filter (GIF) Model 963. These revealed that, in the areas viewed, the jet-polished specimens were generally between 170 nm and 240 nm thick (average 205 nm) with a foil wedge angle between 1° and 2°.

Simultaneous ion irradiation and TEM observation were carried out in the MIAMI-2 system (Microscope and Ion Accelerators for Materials Investigations) at the University of Huddersfield [5] with (singly--charged) 300 keV Ni ions incident on the specimens at 18.6° to the electron beam. Most experiments took place at 475°C but individual experiments were also carried out at temperatures of 375°C, 250°C and 25°C, in all cases using a Gatan Model 652 double-tilt heating holder. The TEM observations were carried out using a modified Hitachi H-9500 microscope [5] operating at 300 kV. All images and videos of these experiments were recorded using a Gatan OneView camera. In MIAMI-2, the ion beam irradiates an area (a spot of diameter ≈ 1 mm) larger than the area irradiated by electrons during the experiments (typically a spot a few microns in diameter). A comparison of the areas irradiated and not irradiated with electrons can thus be used to determine any additional effects that the co-irradiation with electrons may induce. No differences were seen in any of the experiments reported here.

Post-irradiation analysis of the grains that were observed to form was carried out in a JEOL JEM-3010 TEM operating at 200 kV and equipped with a Gatan Orius SC-1000 Model 832 CCD camera using Nano-Beam Diffraction (NBD) with a convergence semi-angle of approximately 2.5 mrad and a nominal spot size of 25 nm. Because of the small size of the

CCD array in the camera (15 mm x 15 mm) and the available range of camera lengths in diffraction mode, it was not possible to capture a sufficient "area" of reciprocal space to carry out the required measurements with the microscope operating normally. The microscope was therefore operated with the projector lens and intermediate lens 2 turned off. This enabled diffraction and Kikuchi patterns with an angular span of approximately 100 mrads to be recorded.

3. Results

3.1. Development of extended defects

Fig. 1a) shows the damage and ion distributions resulting from irradiation of Ni with 300 keV Ni ions as calculated using the Monte-Carlo code SRIM (The Stopping and Range of Ions in Matter) [6]. The calculations used the so-called "Quick", method as advocated by Stoller et al. [7] using an average displacement energy for Ni of 40 eV. The curves show the calculated damage in units of displacements per atom (DPA) and implanted Ni atoms, in atomic parts per million (APPM), per 10^{15} ions/cm^2. (Note that damage to a level of 1 DPA means that, on average, every atom of the irradiated material has been displaced once off its lattice site.)

Fig. 1b) is a schematic illustration of a thin metal foil that has been jet-polished to perforation resulting in a radial profile that is wedge-shaped as shown by the "cut-away" in Fig. 1b) (i). Fig. 1a) indicates that, under ion irradiation, a damaged layer is formed, the majority in the top 150 nm of the Ni specimen and such damage build-up in unconstrained material would cause it to swell in all directions. However, where the damaged layer is constrained by an undamaged underlying layer, lateral stresses will build up in the specimen as indicated by the arrows in Fig. 1b (ii), and these will give rise to a bending of the specimen as shown in Fig. 1b) (iii). Under continued ion irradiation this means that, as point defects form and agglomerate into extended defects, their behaviour will be influenced by the developing stress field.

Fig. 2 shows three sequences of bright-field (BF) TEM images, captured from a digital video recording at 10 frames per second (fps), of the first 12 minutes of an experiment in which a Ni foil was irradiated with 300 keV Ni ions at a temperature of 475°C and with a flux of ≈8.1 × 10^{12} ions/cm^2/s. Each row in this figure will be discussed separately.

In the top row of the image, frames recorded during approximately the first two minutes of irradiation are shown, where panel 2a) shows the specimen just before irradiation commences, 2b) after a fluence of 2.4 × 10^{14} ions/cm^2 and 2c) after a fluence of 9.7 × 10^{14} ions/cm^2. In the experiment, the bend contours, visible in various orientations prior to irradiation in panel 2a), are seen to orient themselves approximately along a ⟨110⟩ direction in panel 1b) as can be seen by comparison with the inset diffraction pattern which shows that the specimen was oriented close to a ⟨111⟩ zone. (Note that the intrinsic rotation between image and diffraction pattern in the Hitachi H-9500 TEM is 0.3° with the diffraction pattern rotated clockwise w.r.t. the image. This rotation has not been corrected in the inset diffraction pattern). The edge of the foil which can be seen at the bottom left of panel 2b) is also approximately parallel to ⟨110⟩. In panels 2b) and 2c), bands, delineated by different diffraction contrast, begin to become visible and, as will be shown below, these features are the origin of the elongated grains which form at higher fluences; the alignment of the boundaries now being between ⟨110⟩ and ⟨120⟩. The evolution of these bands can be seen clearly in the video recording in the Supplementary Material (SM) p1.

Clearly visible from the onset of irradiation is so-called black-spot contrast with spots which grow under continued irradiation and many of which, by their behaviour (to be discussed below), are likely to be (or develop into) small interstitial-type dislocation loops. It is expected that small (<5nm) Stacking-Fault Tetrahedra (SFT) are also formed; however, the imaging conditions (in-focus, bright-field diffraction contrast) were not conducive to providing images of these defects which are generally observed under so-called "weak-beam" conditions [8,9]

Similar processes have recently been observed in Molecular Dynamics (MD) computer simulations of 5 keV Ni recoils in Ni by Granberg et al. [10] and in MD simulations carried out in the current work and described in Section 4 below. The video recordings of the TEM image during irradiation (SM p2) show complex behaviours taking place which include the creation of loops, their motion, disappearance (e.g by losses at surfaces) and coalescence with other loops eventually to form dislocation lines. This latter process can be seen in the middle row – panels 2d), 2e) and 2f) – in which this agglomeration of loops (visible as black spots) can be seen to give rise to a dislocation line which is aligned approximately along a <110> direction. This contrast is consistent with the expected edge dislocation in Ni with a Burgers vector of $^1/_2$<110>.

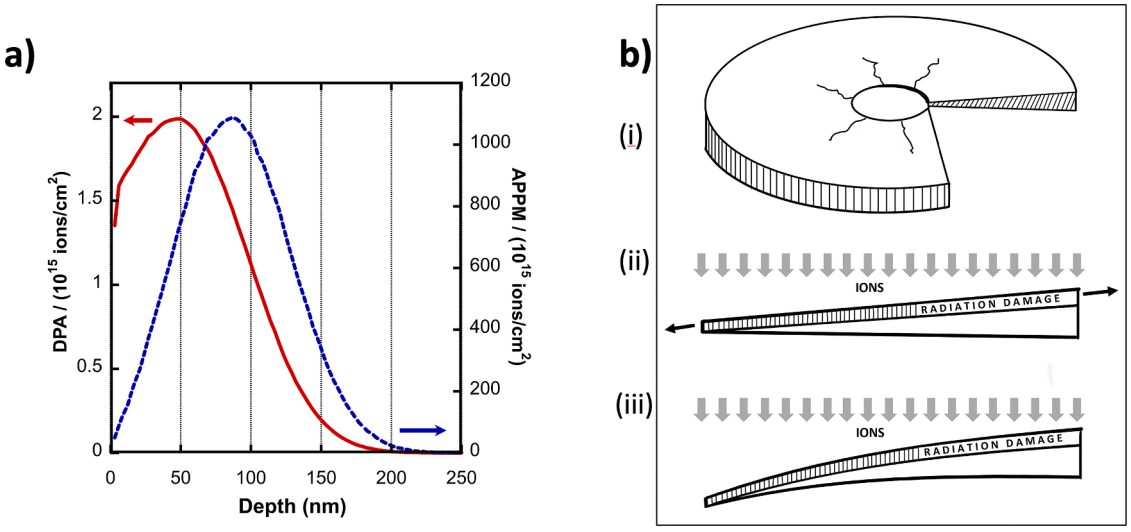

Fig. 1. a) Profiles of damage and implanted ions resulting from irradiation of Ni specimen with 300 keV Ni ions to a fluence of 10^{15} ions/cm^2 calculated using the so-called "Quick" method in SRIM [6] as recommended by Stoller [7]. Left-hand arrow indicates scale for continuous (red) damage curve – right-hand arrow indicates scale for dashed (blue) implanted-ion range curve; b) Schematic illustration of the deformation of a radially wedged TEM foil due to radiation damage. i) Cut-away shows specimen profile; ii) Build-up of lateral stress due to swelling in irradiated layer being constrained by underlying unirradiated region. Arrows indicate the tensile stress applied to the underlying unirradiated material; iii) Resulting bending of the specimen. (For interpretation of the references to colour in this figure legend, the reader is referred to the web version of this article.)

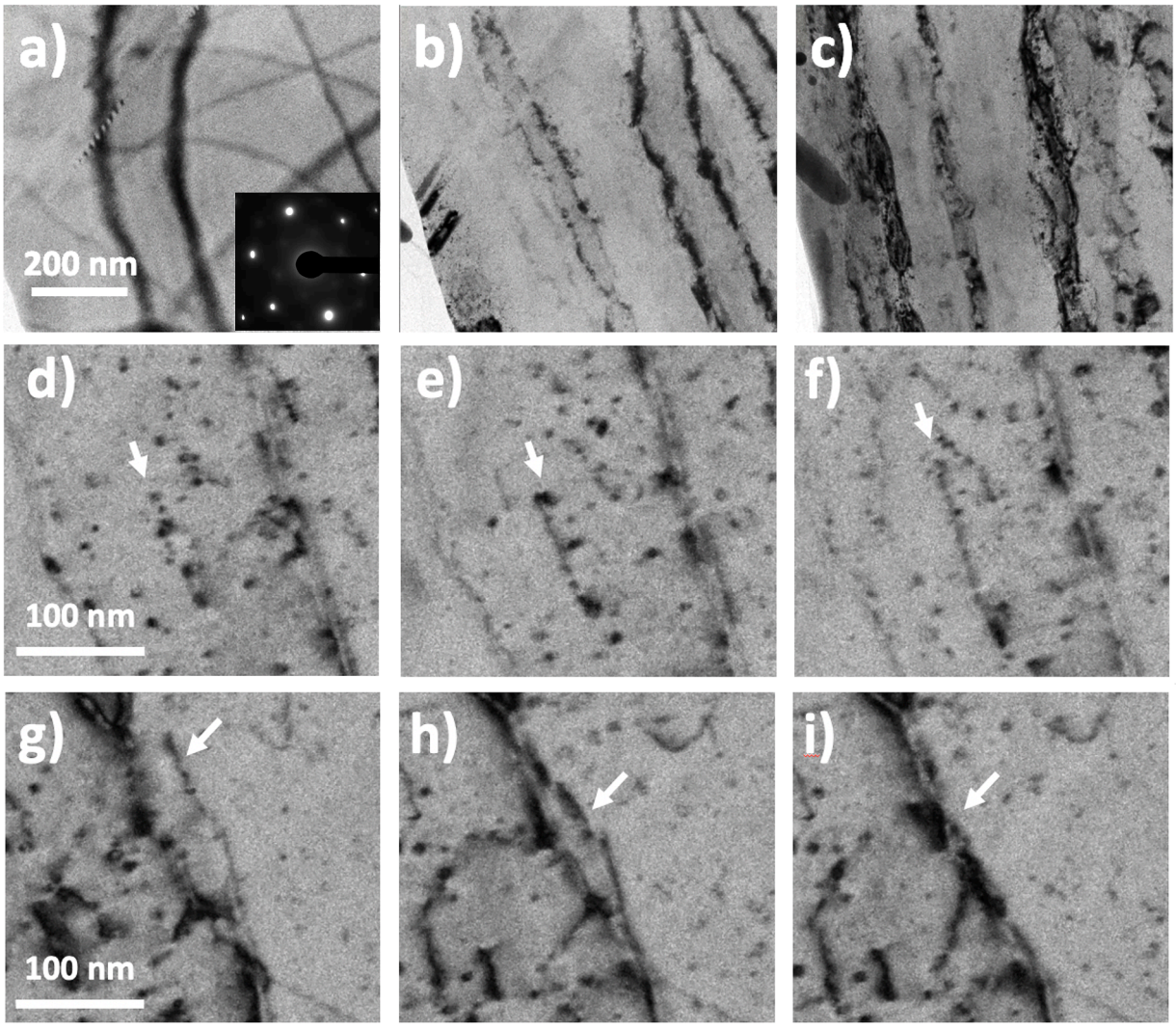

Fig. 2. Bright-field TEM images recorded during irradiation of a Ni foil with 300 keV Ni ions at a temperature of 475°C. Top row: a) before irradiation; b) following irradiation to a fluence of 2.4×10^{14} ions/cm^2; c) following irradiation to a fluence of 9.7×10^{14} ions/cm^2. Middle row: Agglomeration of small dislocation loops into a dislocation line. Following irradiation to a fluence of d) 5.6 x 10^{15} ions/cm^2; e) 5.7×10^{15} ions/cm^2; f) 5.8 x 10^{15} ions/cm^2. Bottom row: Merging of line dislocation into boundary at a fluence of: g) 3.5×10^{15} ions/cm^2; h) Incremental fluence, since 2g), of 5.7×10^{13} ions/cm^2; i) Incremental fluence, since 2h), of 8.1×10^{11} ions/cm^2. The flux in these experiments was 8.1×10^{12} ions/cm^2/s. The scale markers apply to all images in the row. Inset diffraction pattern applies to all images and indicates specimen orientation.

These three images were recorded over a period of 27 seconds, representing a fluence increment between panels d) and f) of 2.2×10^{14} ions/cm^2

Fig. 2g), h) and i) show three successive images with panel g) recorded at a fluence of 3.5×10^{15} ions/cm^2 and panel h) recorded after an additional fluence of 5.7×10^{13} ions/cm^2. Panel i) was recorded a single video frame (at 10 fps) after panel h). The incremental fluence here was thus 8.1×10^{11} ions/cm^2. The images show the movement of the dislocation towards – and its alignment with – a feature that ultimately becomes a LAGB. The dislocation movement is not continuous, with the image in panel h) remaining relatively static for 23 video frames (2.3 seconds) before aligning with the boundary in a single frame (0.1s). Note that all of the observed processes cease within ≈ 1 second of the ion beam being turned off.

Following irradiation of specimens to fluences of approximately 10^{16} ions/cm^2 (at 475°C) the bands initially visible at low fluences, such as in Fig. 2c, and whose boundaries generally repositioned themselves as defects were initially absorbed into them, were seen to have well-defined boundaries which were relatively (but not totally) static under further irradiation. In general, the LAGB did not form in the thinnest regions of the material and, in specimens where the thickness was determined, were seen in regions with a thickness greater than 150 nm.

Although the focus of the work reported here is on specimens irradiated at 475°C, experiments were also carried out at 25°C, 250°C and 375°C – all on jet-polished, radially wedge-shaped foils and, in all cases, similar defect processes were observed leading to the formation of bands similar to those shown in Fig. 2c). Fig. 3 presents micrographs exhibiting this contrast from experiments at the four temperatures studied. The rate at which defects moved and agglomerated increased with temperature and in experiments at 25°C and 250°C only bands of contrast were formed at the fluences achieved in the experiments of 8.0×10^{15} ions/cm^2 and 1.2×10^{16} ions/cm^2, respectively, as shown in Fig. 3a) and 3b). At 375°C and at 475°C, however, (relatively) stable grain boundaries were formed at similar fluences as shown in Fig. 3c) and 3d).

Finally, irradiation of a FIB lamella of single-crystal Ni, ≈ 220 nm in thickness in the electron transparent region (as measured by EELS), and with approximately parallel top and bottom surfaces was also carried out under the same ion-beam conditions at a temperature of 475°C. In this case, although the formation of dislocation loops and their coalescence into dislocation lines occurred, there was no tendency of the bend

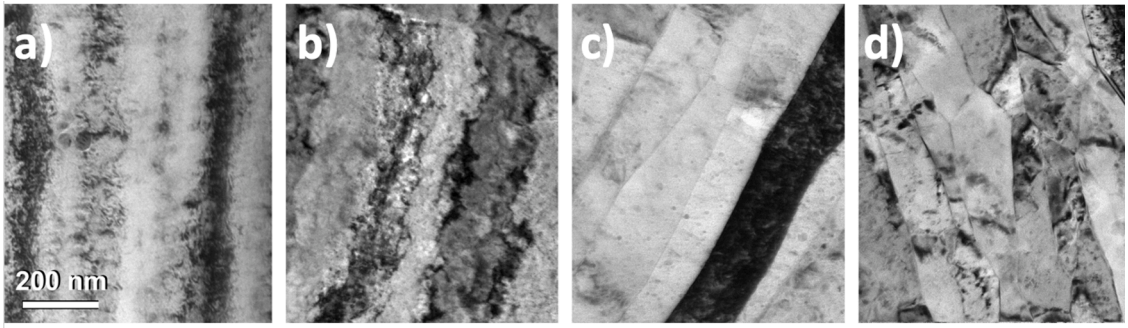

Fig. 3. Bright-field TEM images recorded during irradiation of a Ni foil with 300 keV Ni ions respectively at temperatures and fluences of a) 25°C, 8 × 10^{15} ions/cm^2; b) 250°C, 1.2 × 10^{16} ions/cm^2; c) 375°C, 1.1 × 10^{16} ions/cm^2; d) 475°C, 1.1 × 10^{16} ions/cm^2.

contours to become parallel and no formation of bands or grain boundaries was observed up to a fluence of 1.6 × 10^{16} ions/cm^2. For comparison with the images shown in Fig. 3, a BF image recorded during this experiment is shown in Fig. 4.

3.2. Nano-beam diffraction analysis of grains

Fig. 5a) shows an area of a specimen that was initially monocrystalline over an area significantly larger than the field of view, with the electron beam oriented close to a ⟨100⟩ direction. The image was recorded, at room temperature, following irradiation at 475°C with 300 keV Ni ions to a fluence of 1.0 × 10^{16} ions/cm^2. The numbers indicate five regions separated by grain boundaries formed during the irradiation. A determination of the relative orientation of the material in these regions was made using NBD in a JEOL JEM-3010 TEM with operating conditions as described in Section 2.

The NBD analysis was carried out on each of the five regions shown in Fig. 5a) at room temperature using a 200 keV electron beam with a convergence semi-angle of ≈ 2.5 mrad and a nominal spot size of 25 nm. Under these converged-beam conditions it was possible to record a diffraction pattern containing not only the diffraction discs from Bragg diffraction but also the weaker Kikuchi pattern that results from the Bragg diffraction of electrons that have been incoherently scattered. Two separate exposures of different durations were recorded for each grain and then superimposed; the longer exposure to record the Kikuchi lines and the shorter exposure to record the diffraction discs without undue saturation.

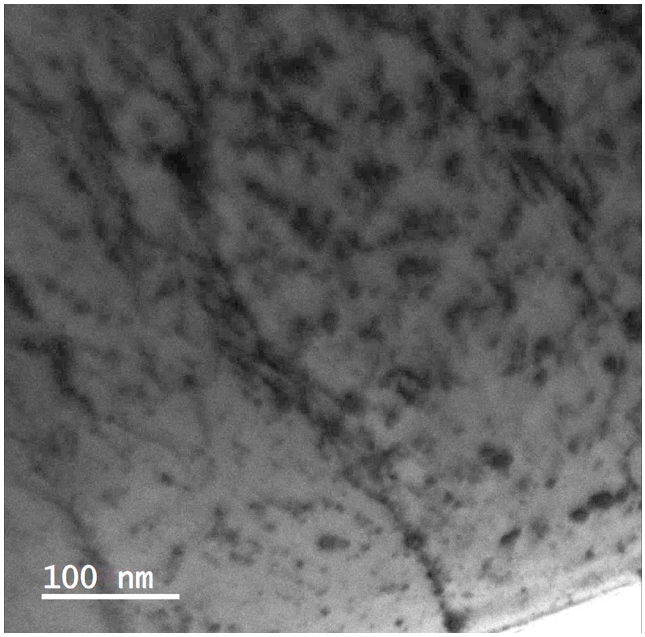

Fig. 4. Bright-field TEM image recorded following irradiation of a Ni FIB lamella with 300 keV Ni ions at a temperature of 475°C at a fluence of 1.6 × 10^{16} ions/cm^2.

These images were then combined to form a pseudo double-exposure image. Using these images, it was possible to determine both the position in reciprocal space of the transmitted electron beam ("000 spot") and the centre of the Kikuchi pattern, which defines the position in reciprocal space of the zone axis of the single crystalline material being probed. Using the Ni Bragg angle for {200} planes as a calibration (7.12 mrad), it was thus possible to determine the angle through which each grain was tilted away from the 000 orientation and thereby determine the relative angles between the grains.

Fig. 5b) shows the double-exposure NBD image obtained from grain 1 on which the 000 position is marked with a "+" and the centre of the Kikuchi lines is marked with a circle and the number 1. The positions of the Kikuchi centres for grains 2 to 5 were also measured on similar images and these have been transferred to Fig. 5b) and also marked by numbered circles. A least-squares fit has been made to these measurements which yields a mean direction of tilt (i.e. the direction normal to the tilt axis) close to being along ⟨120⟩ in this case, (dashed line on Fig. 5b). The measured angles between grains along that tilt direction varied from 0.2° to 1.3° and are indicated on the schematic diagram in Fig. 5c).

4. Molecular dynamics simulations

4.1. Methods

In order to shed light on the development of extended defects in Ni with a constraining layer and at fluences where there is considerable overlap of cascades, MD simulations have been carried out with the code PARCAS [11–13]. The interatomic potential was from Bonny et al. [14], and the cell was 140 unit cells in all three directions ((100),(010),(001)), leading to almost 11 million atoms. The cell had open surfaces in x- and z-directions and was periodic in the y-direction as shown in Fig. 6. In a few x-y planes at the bottom of the cell, atoms were rigidly fixed, to mimic the constraining unirradiated bulk material in the experimental work. The open surfaces mimicked to a degree the "boundary conditions" of the experiments in which the irradiated layer is free to expand into the central hole (the x-direction in Fig. 6) and "upwards" (the z-direction in Fig. 6). Two simulations were carried out to obtain some variation in the results.

The simulations consisted of 30 keV cascades with significant spatial overlap in an initially pristine cell and were conducted at 750 K (477°C), corresponding to the experiments. Random atoms in the centre third of the cell in the x- and z-directions, and randomly in the y-direction were chosen, and given the energy in a random direction. This ensured a fairly homogeneous "irradiation", with minimal surface effects of the

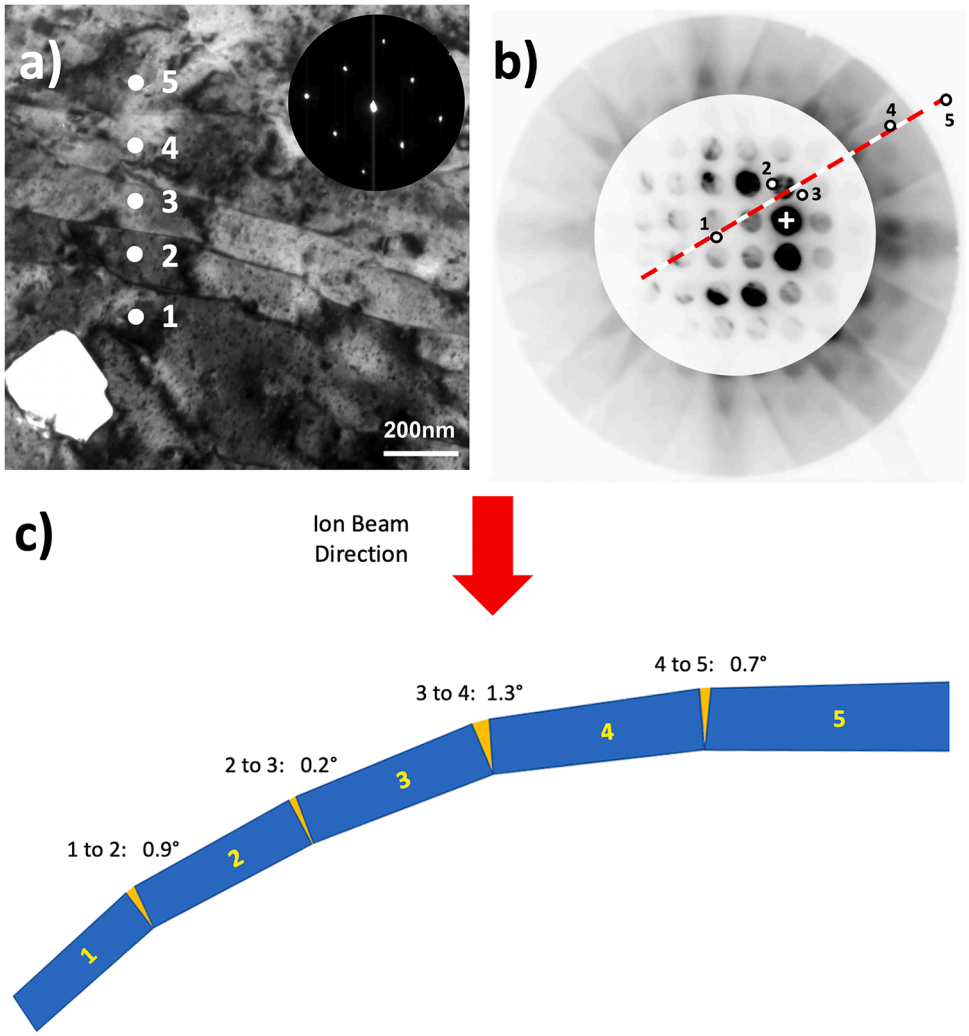

Fig. 5. a) Bright-field TEM image recorded following irradiation of a Ni foil with 300 keV Ni ions at a temperature of 475°C to a fluence of 1.6×10^{16} ions/cm^2. Specimen has been cooled to room temperature. Numbers indicate grains examined using NBD (see text for details). Inset diffraction pattern indicates overall specimen orientation. b) Double exposure image showing diffraction spots and Kikuchi pattern for grain 1. The "+" indicates the 000 reflection. The numbered circles show the centres of the Kikuchi pattern (relative to the diffraction pattern) as measured for all five grains. The dotted line is a least squares fit to the data (assuming that the grains are tilting on parallel axes). Note that this figure has been rotated by ≈ 32° clockwise w.r.t. Fig. 4a) in order to bring the ⟨100⟩ directions into vertical and horizontal alignment on the page. c) Schematic representation of the grain tilting process with measured angles between grains indicated on the figure.

cascades, as the primary interest was in the bulk damage. The simulations were carried out in a two-step manner; firstly a cascade simulation with only border cooling above the fixed atoms, and then a thermalisation with a thermostat on all atoms, to avoid possible overall heating during the series. [15,16]. 2500 impacts were simulated to reach a sufficient simulated dose to yield large defect structures.

All simulations were analysed visually by OVITO [17], to observe physical dimension changes, particularly swelling, and with the Dislocation eXtraction Algorithm (DXA) [18] to extract dislocation structures, also implemented in the same software. In Ni and other FCC metals it is energetically favourable for the perfect 1/2[110] loop to decompose into two 1/6[112] Shockley partials, which is observed in our analysis of the simulations.

4.2. Results

The simulations showed that dislocation structures started to form at low doses and evolved as the dose increased. Fig. 7 illustrates some typical results from this work in which the boundaries of the extended defects have been extracted using DXA and identified and colour coded. At low doses, SFT, small Shockley-partials and small Frank loops are formed. The number of SFT steadily increases, and the number and size of the isolated Frank loops increase to some extent. The main evolution is that of the mobile isolated Shockley partial loops which combine to form larger and larger loops so that at the end of the simulations, there is one large Shockley partial loop, and some intermediate and smaller isolated ones. A snapshot of the dislocation structure at the highest "fluence" is presented in Fig. 8 for one of the two cases for which the full evolution is shown in SM p4. (A snapshot of the dislocation structure at the highest "fluence" in the second case is shown in SM p5). The dislocation density is quite stable after 2000 PKAs in the systems, so that the cells no longer dramatically change at this stage. The volume swelling observed is low, only on the level of a few tenths of a percent (although the surfaces become rough, due to some sputtering and recombination of dislocation loops). Even though there were thermal fluctuations, especially in one of the two cases, a significant number of atoms were observed to be in positions outside of the original cell as the "fluence" increased, indicating a small swelling in the open directions.

A large number of SFT are observed in the simulations and, as mentioned above, these are not generally observed in the bright-field TEM images recorded in the experiments. These were not the focus of this research but further work will be undertaken to compare the

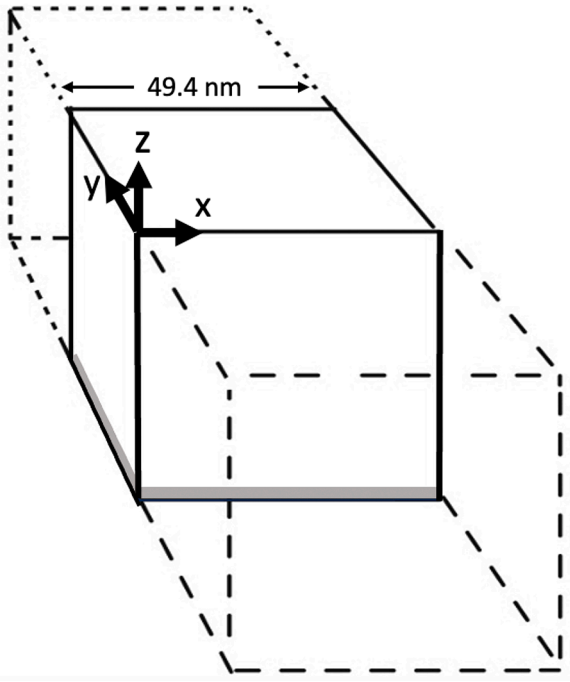

Fig. 6. Schematic illustration of MD cascade simulation. Dotted lines illustrate the periodic boundary conditions in the y direction. Shading at the bottom of the cell indicates constrained atomic layers.

number of SFT in the experiments with those in the simulations.

Looking closely at the large Shockley partial loop formed in this simulation, of which various projections are shown in Fig. 8, it can be seen that this loop has the smallest footprint when viewed along the periodic y-direction, with larger footprints when viewed along the x- and z-axes and along the [101] direction. The habit plane of the loop would, thus, appear to be largely in the (101) plane – giving rise to expansion in an "open" direction. In the second simulation (see SM p4) the footprint of the loop was again smaller when viewed along the periodic y-direction (compared to the open x- and z- directions). The computationally intensive nature of these large MD simulations precludes providing a statistical analysis of the habit-planes of the large loops that form. They do, nonetheless, provide an indication that as Shockley partial loops develop, in this configuration in which the "irradiated" layer is constrained by underlying "unirradiated" material, they will preferentially align with their Burgers vectors favouring a ⟨110⟩ direction oriented towards an open surface. In the context of the experimental observations, as the loops merge to form line dislocations and these then align to form grains, the normal to the grain boundary will thus be preferentially oriented towards an open surface – which, in this case is a radial direction towards the jet polished hole in the specimen.

5. Discussion

The MD simulations showed the development of small loops of different types and their motion, agglomeration and growth into larger loops similarly to that seen in the experiments and indicated that it is likely that, as large Shockley partial loops develop, they will be preferentially oriented with Burgers vectors along open directions – which in the experiments are the radial directions (i.e. towards the central hole). Such a preferential orientation, as the loops agglomerate and ultimately become line dislocations, will give rise to stresses in the implanted layer and bending of the constrained material as observed. The presence of dislocations in a material under stress is known to give rise to the possibility of LAGB formation [19]. Fig. 9a) illustrates schematically the rearrangement that may take place under applied stress and Fig. 9b) shows the way in which the formation of an array or wall of dislocations leads to the formation of the grain boundary – essentially by inserting a wedge-shaped section of material into the original grain.

The formation of LAGB in elemental materials under irradiation, however, does not appear to have been previously reported in the literature. In the more complex materials and radiation environments that occur for instance, in nuclear fuels, irradiation-induced LAGB formation has been identified by Sonoda et al. [4] but, in this case the piling-up of dislocations to form the boundary in UO_2 under neutron irradiation at 1000°C is attributed to initiation by interaction with fission-product precipitates. In the current experiments involving only Ni, it appears that the process illustrated in Fig. 9 can operate at temperatures as low as 25°C as the banding which is the precursor to LAGB formation was seen in all experiments. As both glide and climb are necessary to enable the rearrangement of dislocations to form the LAGB then the Frenkel defects (specifically the mobile interstitials) produced by the ion irradiation presumably enable the climb to occur; however, in this case there are no extrinsic defects such as fission gas bubbles or precipitates to initiate the process.

The build-up of radiation damage in the form of interstitial-type dislocation loops in the implanted layer inevitably causes lattice expansion by introducing a stress field with compressive force in this layer (essentially too many interstitials/too much inefficient stacking) which then applies a tensile force to the top of the unimplanted region. This creates a driving force on the expanding interstitial loops to move down away from the compressive ("crowded") region. Taking the {111}

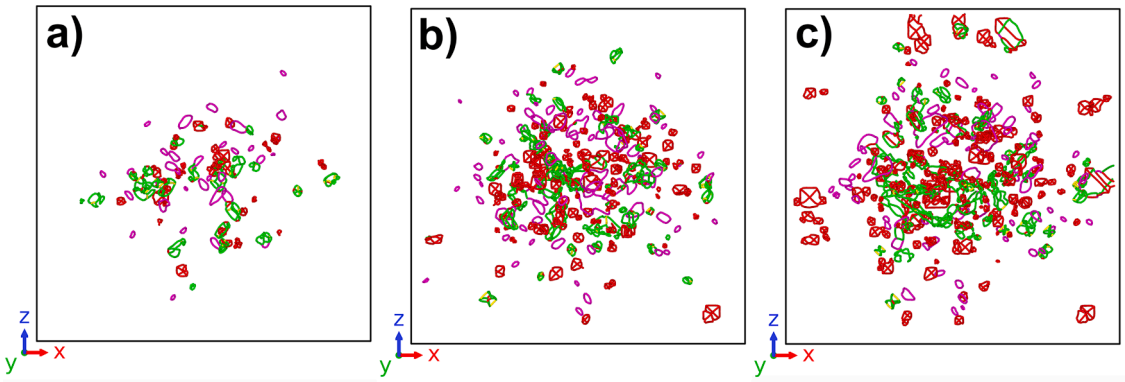

Fig. 7. Evolution of the cell in MD simulation viewed along the y-direction after: a) 50; b) 250 and c) 500 initiated PKAs in the same cell. Dislocations extracted using DXA, where green represents Shockley partial, red stair-rod, purple Frank and yellow Hirth dislocation segments. (The stair-rod dislocations form the edges of SFT. Note that these were not visible in the experimental studies). (For interpretation of the references to colour in this figure legend, the reader is referred to the web version of this article.)

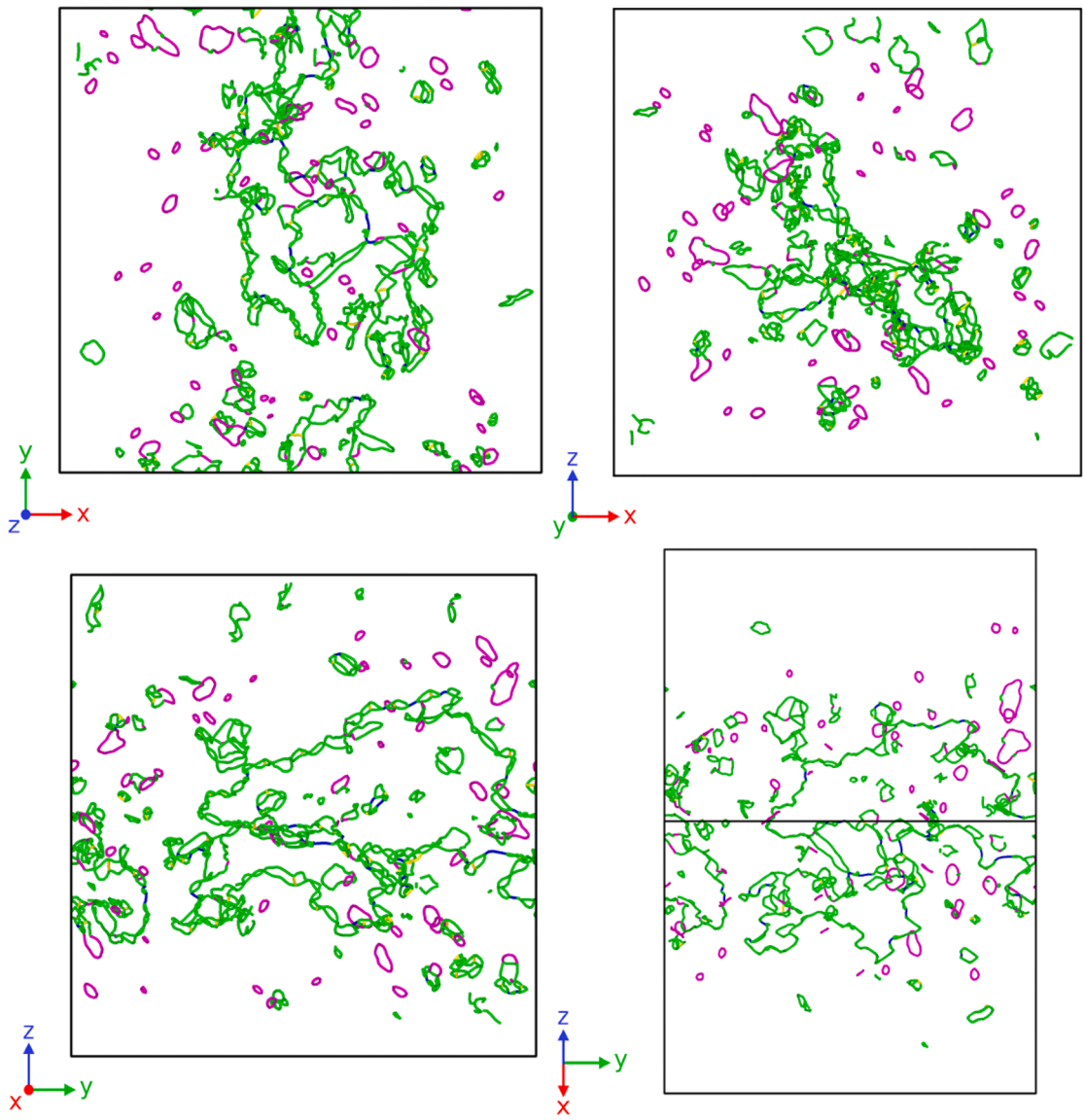

Fig. 8. Dislocation structure from MD simulation from four different orientations at the highest dose. On the left side the two open directions, top right the periodic direction and bottom right from the [101] direction. The green lines represent Shockley partial dislocation segments and the purple lines the Frank loops. The stair-rod dislocations (outlining the SFT) have been removed for clarity. The habit plane of the main dislocation loop is clearly in the [101] direction with a much smaller trace in the periodic direction. (For interpretation of the references to colour in this figure legend, the reader is referred to the web version of this article.)

plane with the highest Schmid factor as the active slip plane in an FCC metal, let us identify the individual {111} plane whose trace meets the intersection between a wall and the lower surface of the TEM sample – this is illustrated as a dotted (blue line) and labelled as the "lower limiting slip plane" for this wall in Fig. 10. The majority of dislocations above this line will glide downwards towards wall 1 (driven by the stress field) and will join that wall. Downward gliding dislocations on slip planes below this line will be lost at the bottom of the specimen.

Once the long-range stress field of wall 1 has reached a certain level, further dislocations may be repelled from it. If this movement is not arrested by meeting another dislocation, it will continue until the dislocation reaches a location where the back stress from wall 1 is matched by the original stress from the implanted region. The depth at which these opposing forces are matched in strength is indicated by the "upper stress boundary" dashed line in Fig. 10. At this sticking point, the probability of meeting and tangling with another dislocation is highest; therefore, another wall (wall 2) is most likely to form here. This process will then repeat to form successive walls.

The separation of the walls (and thus ultimately the width of the new grains) that would be expected from this simplified model can be estimated from geometrical considerations. Specifically, the lateral distance between wall 1 and wall 2 is determined by: the depth of the upper stress boundary; the sample thickness; and ξ, the complementary angle between the operating slip plane and the sample normal which, for a small foil wedge angle (1–2° in this case), is essentially the angle between slip plane and bottom foil surface as shown Fig. 10. The length t is the distance between the upper stress boundary and the bottom surface of the TEM sample. The wall spacing would therefore be given by:

$$w = t/tan\xi.$$

The distance t is not known; however, its upper bound is the distance between the peak in the damage profile and the lower surface of the TEM specimen. Taking the former as 50 nm, from the SRIM-estimated damage profile in Fig. 1a), and the foil thickness of 205 nm (the mean value measured by EELS), this would yield a value of ≈155 nm. The macroscopic starting grains used for the experiments generally had surface normals close to ⟨100⟩, ⟨110⟩ or ⟨111⟩ and considering the angles, ξ, that such foil surfaces make with the {111} slip planes this model would

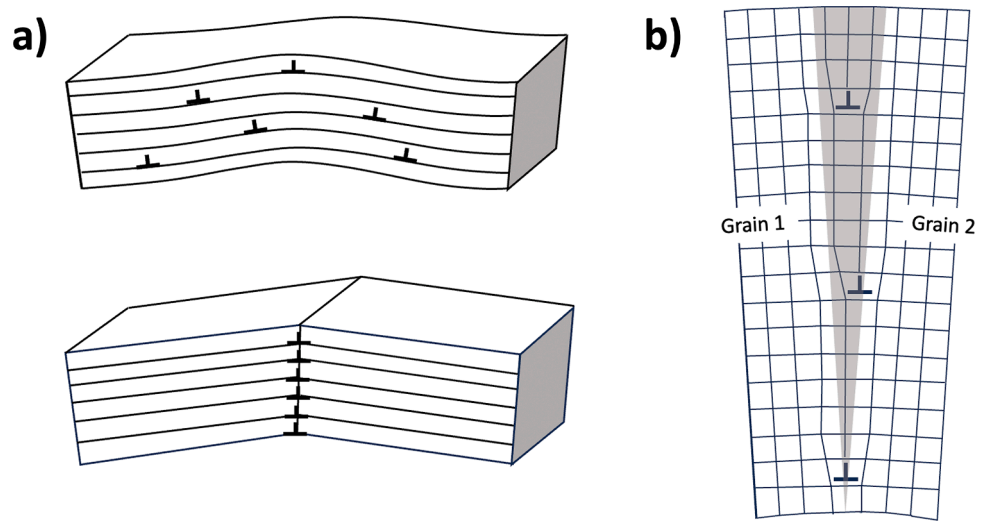

Fig. 9. Schematic representation of the formation of a LAGB by the stacking of dislocations. (After reference [16].) a) Bent crystal with random arrangement of dislocations which rearrange to form a LAGB; b) Detail of stacking of dislocations giving rise, effectively, to the insertion of a wedge-shaped piece of material as indicated by the shading.

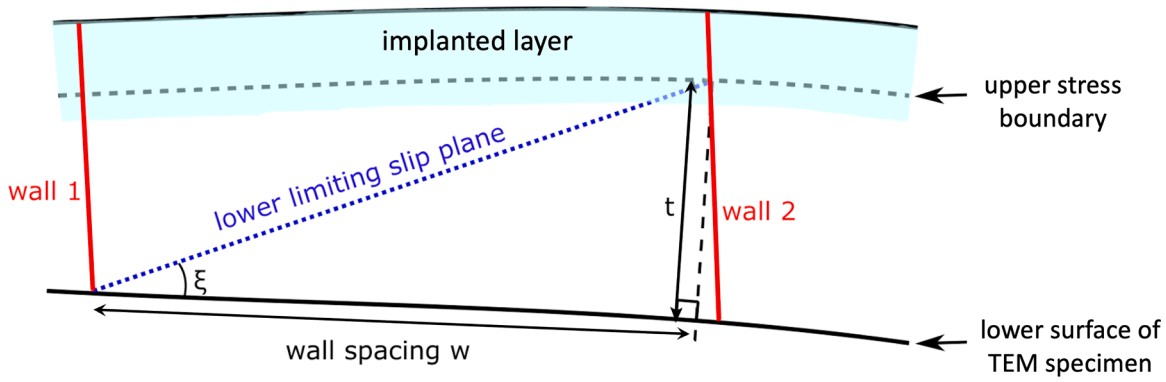

Fig. 10. Schematic diagram of cross-section of the TEM foil, illustrating factors responsible for grain width. (See text for details).

predict an upper limit for w in the range 50 – 200 nm.

Although grain widths are variable and even individual grains did not have a constant width, measurements on 40 grains from 5 different experiments indicted an average grain width of 180 nm with a standard deviation of 58 nm which aligns reasonably with the upper limit estimated above and perhaps indicates that the upper stress boundary in the experiments may be fairly close to the peak in the damage distribution.

The total number of Ni atoms per unit specimen area, N_{wedge}, in the wedge-shaped volumes that have been added to the material to give rise to the grain boundaries (and assumed to have an equilateral cross-section as illustrated in Fig. 8b) is given by:

$$N_{wedge} = (N_g - 1)\rho L d^2 \tan(\theta/2)$$

where N_g is the number of grains per unit area, L is the width of that area, ρ is the atomic density, d is the foil thickness, and θ is the angle of the wedge; (the volume of the wedge, V, being given by:

$V = Ld^2\tan(\theta/2))$.

As indicated above, the mean grain width was 180 nm and thus $N_g =$ 55,556 grains/cm^2 (assuming that the grains span the full width of the area studied). Taken together with a foil thickness of 205 nm, a grain wedge angle of 0.8° (the average of the measurements in Fig. 4) and the maximizing assumption that the density of the material in the wedge is that of the matrix, this yields a value: $N_{wedge} \approx 1.5 \times 10^{16}$ atoms/cm^2. Note that, in reality, the atomic density in the boundary will be somewhat less than that of the matrix and the precise value is not known; however, it is interesting to note that the estimated number of Ni atoms forming the wedges ($\leq 1.5 \times 10^{16}$ atoms/cm^2) would appear to be fairly close to the number of additional Ni atoms (1.6×10^{16} atoms/cm^2) injected into the foil in the experiment in which the angles between grains were measured. The closeness of the estimated number of atoms in the grain-boundary wedges to the number of injected Ni atoms is likely to be co-incidental as this number is a small fraction of the total number of interstitials created as displacement damage which, from the SRIM simulations reported above, is of order 1.8×10^{19} atoms/cm^2.

However, there is an example in the literature – the so-called "Si +1 model" [20] – where the "injected" interstitials (due to substitutional defects) appear to account for defect structures remaining after annealing (311 defects). The possibility of similar disproportionate effects due to these excess injected interstitials cannot be completely ruled out and will only be resolved through similar experiments involving irradiation with other species.

This does serve to indicate, however, that a large fraction of the interstitials created in the collision cascades must recombine with vacancies or be lost to surfaces under our experimental conditions (and we note that the proximity of two surfaces in the in-situ experiments may lead to defect dynamics that differ quantitatively from those in bulk materials).

Vacancies that have not recombined or been lost to the surface may agglomerate during the experiments into small clusters or be incorporated into SFT. These latter were observed in the MD simulations

reported in Section 4 but these will generally not be visible under the bright-field, in focus, imaging conditions used in the present work as these are best studied under weak-beam dark-field conditions [8,9].

6. Conclusions

Self-ion irradiation at 300 keV of monocrystalline regions of Ni foils, with wedge-shaped radial cross-sections, to fluences of order 1.0×10^{16} atoms/cm^2 at a temperature of 475°C has been observed to give rise to the formation of elongated grains (≈ 180 nm in width and microns in length) with their long axes approximately parallel to the foil edge. Angles between grains have been measured to be up to 1.3°. Interstitials formed by the irradiation initially agglomerate into dislocation loops, the majority of which (from the MD results) are likely to be Shockley partials. Of the possible Burgers vectors of these loops the stress field gives rise to a preferred orientation best aligned with the radial direction (towards the central hole in the foil). These loops then combine to form dislocation lines which, under the continuing influence of the stress (due to the lateral expansion of the irradiated layer constrained by the un-irradiated material), then pile up to form dislocation walls and eventually low-angle grain boundaries. The orientation of the gains, with the long axis approximately parallel to the specimen edge, results from the irradiated region of the foil being unconstrained in the radial direction and thus allowing expansion in this direction. The width of the grains, measured to have a mean value of 180 nm, is determined geometrically by the interaction between the stress field of the developing dislocation walls and that from the lateral expansion of the irradiated layer and the angle between active slip planes and the foil normal.

The observed band formation that ultimately gives rise to grain formation at 375°C and 475°C was also observed (albeit occurring at a slower rate) at temperatures of 25°C and 250°C but full grain formation was not observed at these temperatures within the fluence range studied. (Generally up to ≈ 10^{16} ions/cm^2). Low angle grain boundaries were not observed in the thinner regions of the foil (i.e. < 150 nm) which, with reference to the damage profile in Fig. 1a)), may imply that an initial dislocation wall forms where there is essentially no underlying unirradiated region and thus no stress field driving further dislocation motion.

The grain formation observed in these experiments occurs as a result of the specific radially wedge-shaped nature of the irradiated foils. However, it seems likely that this type of grain formation under displacing irradiation may occur in other situations where differential stresses develop leading to differential expansion such as where there are interfaces between different materials under irradiation.

CRediT authorship contribution statement

S.E. Donnelly: Writing – review & editing, Writing – original draft, Project administration, Investigation, Formal analysis, Conceptualization. **G. Greaves:** Writing – review & editing, Investigation. **F. Granberg:** Writing – original draft, Visualization, Software, Investigation, Formal analysis. **J. Sharp:** Writing – review & editing, Formal analysis. **A.H. Milston:** Writing – review & editing, Resources. **J.A. Hinks:** Writing – review & editing. **K. Nordlund:** Writing – review & editing, Software.

Declaration of competing interest

The authors declare that they have no known competing financial interests or personal relationships that could have appeared to influence the work reported in this paper.

Acknowledgements

The authors acknowledge funding from the UK Engineering and Physical Sciences Research Council (EPSRC). Specifically, the MIAMI-Facility was constructed with grants EP/E017266/1 and EP/M028283/1; AHM acknowledges a postgraduate grant from the University of Huddersfield's Doctoral Training Programme (EP/T51813X/1) and JS acknowledges postdoctoral funding (EP/T027193/1). FG and KN acknowledge that this work has been partially carried out within the framework of the EUROfusion Consortium, funded by the European Union via the Euratom Research and Training Programme (Grant Agreement No 101052200 – EUROfusion). Views and opinions expressed are however those of the authors only and do not necessarily reflect those of the European Union or the European Commission. Neither the European Union nor the European Commission can be held responsible for them. Computer time granted by the IT Center for Science (CSC), Finland is gratefully acknowledged.

Supplementary materials

Supplementary material associated with this article can be found, in the online version, at doi:10.1016/j.jnucmat.2024.155588.

Data availability

Data will be made available on request.

References

[1] G.S. Was, Fundamentals of Radiation Materials Science: Metals and Alloys, Springer-Verlag, Berlin, 2007.
[2] D. Kaoumi, A.T. Motta, R.C. Birtcher, A thermal spike model of grain growth under irradiation, J. Appl. Phys. 104 (7) (2008).
[3] Joseph R. Michael, Focused ion beam induced microstructural alterations: Texture development, grain growth, and intermetallic formation, Microscopy and Microanalysis 17 (3) (2011) 386–397.
[4] M.Kinoshita T.Sonoda, T.Wiss I.L.F.Ray, D.Pellottiero H.Thiele, Hj.Matzke V.V. Rondinella, Transmission electron microscopy observation on irradiation-induced microstructural evolution in high burn-up UO2 disk fuel, Nucl. Instrum. Methods. Phys. Res. B 191 (2002) 622–628.
[5] G. Greaves, A.H. Mir, R.W. Harrison, M.A. Tunes, S.E. Donnelly, J.A. Hinks, New microscope and ion accelerators for materials investigations (MIAMI-2) system at the University of Huddersfield, Nucl. Instrum. Methods. Phys. Res. B 931 (2019) 37.
[6] J.F. Ziegler, M.D. Ziegler, J.P. Biersack, SRIM – The stopping and range of ions in matter (2010), Nucl. Instrum. Methods. Phys. Res. B 268 (2010) 1818–1823.
[7] R.E. Stoller, M.B. Toloczko, G.S. Was, A.G. Certain, S. Dwaraknath, F.A. Garner, On the use of SRIM for computing radiation damage exposure, Nucl. Instrum. Methods. Phys. Res. B 310 (2013) 75–80.
[8] R. Schaüblin, Z. Yao, N. Baluc, M. Victoria, Irradiation-induced stacking fault tetrahedra in fcc metals, Phil. Mag. 85 (2005) 769–777.
[9] M.L. Jenkins, M.A. Kirk. Characterisation of Radiation Damage By Transmission Electron microscopy, (2000) CRC Press p55 and p72.
[10] F. Granberg, K. Nordlund, M.W. Ullah, K. Jin, C. Lu, H. Bei, L. M. Wang, F. Djurabekova, W. J. Weber, Y. Zhang, Mechanism of radiation damage reduction in equiatomic multicomponent single phase alloys, Phys. Rev. Lett. 116 (2016) 135504.
[11] K. Nordlund, Molecular dynamics simulation of ion ranges in the 1–100 keV energy range, Comput. Mater. Sci. 3 (4) (1995) 448–456.
[12] M. Ghaly, K. Nordlund, R.S. Averback, Molecular dynamics investigations of surface damage produced by kiloelectronvolt self-bombardment of solids, Phil. Mag. A 79 (4) (1999) 795–820.
[13] K. Nordlund, M. Ghaly, R.S. Averback, M. Caturla, T. Diaz de la Rubia, J. Tarus, Defect production in collision cascades in elemental semiconductors and fcc metals, Phys. Rev. B 57 (1988) 7556–7570.
[14] G. Bonny, N. Castin, D. Terentyev, Interatomic potential for studying ageing under irradiation in stainless steels: the FeNiCr model alloy, Modelling Simul. Mater. Sci. Eng. 21 (2013) 085004.
[15] F. Granberg, K. Nordlund, M.W. Ullah, K. Jin, C. Lu, H. Bei, L. M. Wang, F. Djurabekova, W. J. Weber, Y. Zhang, Mechanism of radiation damage reduction in equiatomic multicomponent single phase alloys, Phys. Rev. Lett. 116 (2016) 135504.
[16] F. Granberg, J. Byggmästar, K. Nordlund, Molecular dynamics simulations of high-dose damage production and defect evolution in tungsten, J. Nucl. Mater. 556 (2021) 153158.
[17] A. Stukowski, Visualization and analysis of atomistic simulation data with ovito-the open visualization tool (2010), Modelling Simul. Mater. Sci. Eng. 18 (2010) 015012.

[18] A. Stukowski, V. Bulatov, A.Arsenlis A.Vasily, Automated identification and indexing of dislocations in crystal interfaces, Modelling Simul. Mater. Sci. Eng. 78 (20) (2012) 085007.
[19] D. Hull, Introduction to Dislocations, Pergamon Press, 1975, p. 34. ISBN 0-08-018129-5197.
[20] D.J. Eaglesham, A. Agarwal, T.E. Haynes, H-J. Gossmann, D.C. Jacobson, J. M. Poate, Damage and defects from low-energy implants in Si, Nucl. Instrum. Methods. Phys. Res. B 120 (1-4) (1996) 1–4.